Colloids and Surfaces B: Biointerfaces 239 (2024) 113934

Contents lists available at ScienceDirect

Colloids and Surfaces B: Biointerfaces

journal homepage: www.elsevier.com/locate/colsurfb

Non-invasive paper-based sensors containing rare-earth-doped nanoparticles for the detection of D-glucose

Gabriel López-Peña [a], Eva Ortiz-Mansilla [b], Antonio Arranz [a], Nicoleta Bogdan [c], Miguel Manso-Silván [a,d], Emma Martín Rodríguez [a,e,*]

[a] Departamento de Física Aplicada and Instituto de Ciencia de Materiales Nicolás Cabrera, Universidad Autónoma de Madrid, C/ Francisco Tomás y Valiente 7, Madrid 28049, Spain
[b] Departamento de Física Teórica de la Materia Condensada, Universidad Autónoma de Madrid, C/ Francisco Tomás y Valiente 7, Madrid 28049, Spain
[c] Department of Chemistry and Biochemistry, Concordia University, Montreal, QC, Canada
[d] Centro de Micro-Análisis de Materiales, Universidad Autónoma de Madrid, C/ Francisco Tomás y Valiente 7, Madrid 28049, Spain
[e] Nanomaterials for BioImaging Group, Instituto Ramón y Cajal de Investigación Sanitaria IRYCIS, Ctra. de Colmenar km 9,300, Madrid 28034, Spain

ARTICLE INFO

Keywords:
Enzyme-free sensor
Up-converting nanoparticles
Glucose detection
Luminescent sensor
Paper-based sensor
Non-invasive sensing

ABSTRACT

Today, diabetes mellitus is one of the most common diseases that affects the population on a worldwide scale. Patients suffering from this disease are required to control their blood-glucose levels several times a day through invasive methods such as piercing their fingers. Our $NaGdF_4$: 5% Er^{3+}, 3% Nd^{3+} nanoparticles demonstrate a remarkable ability to detect D-glucose levels by analysing alterations in their red-to-green ratio, since this sensitivity arises from the interaction between the nanoparticles and the OH groups present in the D-glucose molecules, resulting in discernible changes in the emission of the green and red bands. These luminescent sensors were implemented and tested on paper substrates, offering a portable, low-cost and enzyme-free solution for D-glucose detection in aqueous solutions with a limit of detection of 22 mg/dL. With this, our study contributes to the development of non-invasive D-glucose sensors, holding promising implications for managing diabetes and improving overall patient well-being with possible future applications in D-glucose sensing through tear fluid.

1. Introduction

Diabetes mellitus is a metabolic alteration characterised by an insulin insufficiency, deriving in high blood-glucose levels (hyperglycaemia), leading to glucose intolerance in diabetic patients [1–4]. The common blood-glucose levels are between 70 and 100 mg/dL, and blood-glucose levels higher than 125 mg/dL are diagnosed as hyperglycaemia [5–10]. Monitoring blood glucose levels several times a day is required, which usually involves piercing the patient's fingers or forearms to collect a small amount of blood [11]. This process presents some disadvantages, such as the appearance of calluses on the patient's finger, discomfort, dilution of blood samples when the patient applies force to the open wound to extract more blood, and excessive consumption of supplies [12,13].

Several non-invasive methods that allow the collection or monitoring of fluids have been investigated over the years. Some of these methods include infrared or Raman spectroscopy [14–16], measuring glucose-induced changes in the polarisation of a laser [17–20], controlling the photoacoustic behaviour of the skin depending on glucose levels [21], optical coherence tomography [22–24], surface plasmon resonance induced changes [25–27], electrical impedance measurements [28–30], and fluorescence measurements [31–33]. In order to achieve a non-invasive technique to measure blood-glucose levels, some of these methods propose the analysis of other physiological fluids, such as saliva, interstitial fluid, sweat, urine or tear fluid [1], being the last one, one of the most promising for the collection of information about patients. The composition of tear fluid provides direct information about corneal biochemistry and physiology, and since tears are generated in the lacrimal glands through filtration from plasma blood, which circulates all around the body, collecting information from different body parts is also possible. Several studies have demonstrated how most of the proteins that make up human plasma can be found in tear fluid, and some of them have even found a relationship with albumin, urea, glucose, and cholesterol concentrations in tears of semi-aquatic,

* Corresponding author at: Departamento de Física Aplicada and Instituto de Ciencia de Materiales Nicolás Cabrera, Universidad Autónoma de Madrid, C/ Francisco Tomás y Valiente 7, Madrid 28049, Spain.
E-mail address: emma.martin@uam.es (E. Martín Rodríguez).

https://doi.org/10.1016/j.colsurfb.2024.113934
Received 24 January 2024; Received in revised form 15 April 2024; Accepted 28 April 2024
Available online 30 April 2024

terrestrial, and marine reptiles [34,35]. Because of this, tear fluid has attracted the attention of the scientific community due to its noticeable potential for the control of several diseases such as cystic fibrosis, Parkinson's, Alzheimer's disease, cancer, sclerosis and diabetes mellitus [36–39]. In addition, the collection of tear fluid can be performed in a few seconds in a non-invasive way, avoiding the discomfort of the patient and being able to collect from nanolitres to microlitres of tear fluid. However, the concentration of products such as glucose that can be found in tear fluid is much lower than the ones found in blood, being this one of the main drawbacks when using body fluids. For this reason, the development of reliable sensors with high sensibility and specificity that can work with these types of fluids is a key point in improving the quality of life of diabetic patients.

Among all the fluorescent sensing probes that can be used for the measurement of blood glucose levels, rare-earth-doped up-converting nanoparticles (UCNPs) stand out due to their unique optical properties, such as narrow emission peaks in the VIS and NIR ranges, long lifetimes in the range of micro and milliseconds, or reduced photobleaching. Moreover, the sensing ability of UCNPs has been proved through the analysis of the changes in their optical properties depending on several factors such as pH, pressure, temperature or being in the presence of high energy vibrational states, making them an excellent choice for sensing applications [40–43]. Another crucial factor to take into consideration when fabricating a sensor is the selection of a suitable substrate, which will directly affect its performance, influencing properties such as the sensitivity, selectivity, or stability. Flexible substrates offer the possibility of developing wearable and disposable sensors because of their properties. Among them, paper stands out since it exhibits good mechanical bendability, durability, and porous characteristics, in combination with its low cost and its easy-to-functionalise character [44–46]. Moreover, the use of paper-based sensors can have a potential effect on the reduction of the high number of consumable supplies used in the traditional techniques to monitor blood-glucose levels.

In this work, UCNPs doped with Nd^{3+} ions acting as sensitisers and Er^{3+} ions acting as activators have been synthesised and integrated in paper-based sensors as a first approach to developing new non-invasive and paper-based enzyme-free luminescence D-glucose sensors. These NPs exhibit intense up-conversion emissions that match the OH vibrational levels of D-glucose, inducing changes in their red-to-green ratio that can be used as a luminescence-based detection mechanism.

2. Materials and methods

2.1. Synthesis of $NaGdF_4$: 5% Er^{3+}, 3% Nd^{3+} nanoparticles

$NaGdF_4$: 5% Er^{3+}, 3% Nd^{3+} nanoparticles were synthesised following a standard thermal decomposition method. A mixture containing 2.5 mmol of $GdCl_3$, $NdCl_3$ and $ErCl_3$ (Alfa Aesar), 25 mL of octadecene (Sigma Aldrich) and 25 mL of oleic acid (Thermo Scientific) was raised to 120 °C in vacuum during 1 h, followed by the addition of 0.85 g of sodium trifluoroacetate (Sigma Aldrich). After this, the temperature was raised to 300 °C for 2 h in an argon atmosphere. The $NaYF_4$ NPs used for comparison in the XPS experiments were synthesised following the same protocol, but instead of $GdCl_3$, YCl_3 was prepared.

2.2. Transmission electron microscopy

Transmission electron microscopy images were obtained in a JEOL JEM1010 microscope (JEOL) operating at 100 kV. The samples were prepared by dropping sample dispersions (0.1–0.5 mg/mL in hexane) onto a 300-mesh carbon-coated copper grid (3 mL in diameter) followed by evaporation of the solvent.

2.3. Dynamic light scattering and ζ-Potential measurements

DLS measurements were made with a Zetasizer Nano ZS instrument (Malvern Panalytical, Malvern) using a 0.1 mg/mL dispersion of NPs in deionised water contained in a standard 1 cm quartz cuvette. The system uses a red laser (630 nm wavelength) as an energy source, and the angle between the sample and the detector was 173°. The ζ-Potential measurements were performed with the same equipment using the Zetasizer Nano Series disposable folded capillary cells (Malvern) and the correct ζ-Potential configuration in the equipment.

2.4. Fourier transform infrared spectroscopy measurements

The Fourier transform infrared (FTIR) spectra presented in this work were measured with an ATR-FTIR module of the Cary 630 FTIR (Agilent) by depositing a droplet of the desired dispersion on the diamond cell and letting the solvent evaporate. After the sensing surface is dry, the tip of the diamond cell was pressed towards the surface.

2.5. Up-conversion emission spectra

Up-conversion emission spectra of the NPs were measured using an 800 nm fibre coupled laser diode (Lumics) to excite the nanoparticles and a FESH750 (Thorlabs) short-pass filter to block all wavelengths below 750 nm. An iHR320 (HORIBA) monochromator and a cooled CCD array Synapse (HORIBA) detector were used to collect the spectra.

2.6. X-ray photoelectron spectroscopy (XPS) measurements

The XPS experiments performed in this work have been carried out in an ultra-high vacuum chamber using a hemispherical analyser (SPECS Phoibos 100MCD-5) and Al Kα (1486.6 eV) radiation from a twin anode (Al–Mg) X-ray source at a constant power of 300 W. For the analysis of the XPS spectra, binding energies (BE) were determined by referencing the C 1 s peak of the C-C species at 284.6 eV.

2.7. Paper-based sensor fabrication

A 10 mg/mL dispersion of $NaGdF_4$: 5% Er^{3+}, 3% Nd^{3+} NPs in deionised water was prepared. 1.5 ×1.5 cm pieces of Whatman chromatography paper (CAT No. 3001–861) were immersed in the NP dispersion for 10 min. During this time, the container with the dispersion of NPs and the piece of paper was placed in a shaker to gently move the container to ensure an even distribution in all the paper. Once this process was completed, the piece of paper was dried in an UN 55 oven (Memmert) at 60 °C for 20 min.

3. Results and discussion

3.1. Morphological and optical characterization

$NaGdF_4$: 5% Er^{3+}, 3% Nd^{3+} NPs (ErNd-NPs) were synthesised following a thermal decomposition procedure, where a mixture of Nd, Er and Gd chlorides, octadecene and oleic acid was raised to 300 °C during 2 h in order to form ErNd-NPs covered with oleate. This ion stoichiometry ensures the most intense emission in both the VIS and NIR ranges, making these NPs suitable for more reliable detection of changes in their red-to-green ratio due to the presence of D-glucose without losing the intensity of NIR emissions for other parallel applications. Fig. 1A presents the statistical analysis of a series of transmission electron microscopy (TEM) images of the synthesised ErNd-NPs, resulting in a medium diameter of 31 ± 10 nm. At first sight, the TEM image in the inset indicates that the synthesised NPs do not show any significant aggregation.

The emission of the NPs was characterised using an 800 nm diode laser to excite the Nd^{3+} ions in the system. Fig. 1B shows the up-

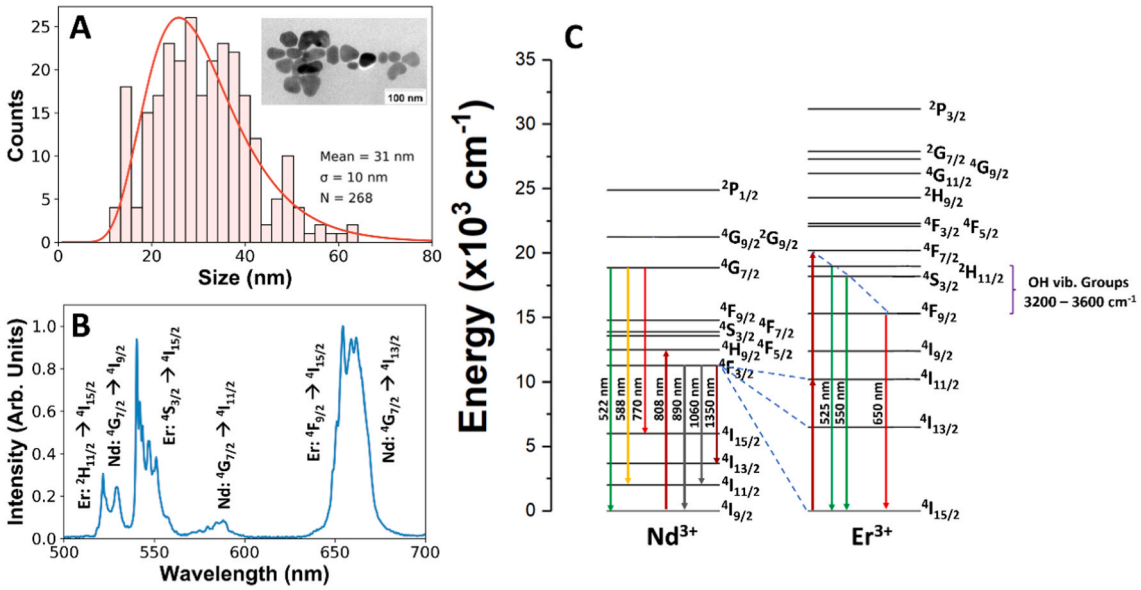

Fig. 1. A. Statistical analysis of TEM images showing a mean diameter of 31 ± 10 nm. The inset shows a TEM image of the synthesised ErNd-NPs with a scale bar of 100 nm. B. Emission spectrum of the ErNd-NPs after excitation with an 800 nm laser. C. Energy level diagram of the ions present in the synthesised ErNd-NPs.

conversion emission spectrum of ErNd-NPs. The different transitions associated with the Nd^{3+} and Er^{3+} ions are shown in their corresponding emission bands. Using 800 nm as excitation, the $^4H_{9/2}$ energy level of Nd^{3+} ions can be easily populated, and since Nd^{3+} present resonant energy levels with Er^{3+} ions, there is a high probability of energy transfer, leading to the population of the $^4F_{7/2}$ energy levels of Er^{3+} (Fig. 1C). From this level, the electrons undergo a nonradiative relaxation to the $^2H_{11/2}$ and $^4S_{3/2}$ levels, from where the $^2H_{11/2} \rightarrow {}^4I_{15/2}$ and $^4S_{3/2} \rightarrow {}^4I_{15/2}$ transitions take place, producing the characteristic green luminescence of Er^{3+}. At the same time, after a nonradiative relaxation to the $^4F_{9/2}$ level, the $^4F_{9/2} \rightarrow {}^4I_{15/2}$ transition can occur, producing the red emission of Er^{3+}. Under normal conditions, there is a low probability of nonradiative decays from the $^2H_{11/2}$ and $^4S_{3/2}$ levels to the $^4F_{9/2}$ level, since the energy separation between these levels is around 3200 1/cm and the phonon energy of the $NaGdF_4$ lattice is approximately 350 1/cm, meaning that, to perform a nonradiative deexcitation, around nine phonons are required. Having this in mind, there is a possibility for the OH groups present in D-glucose to act as a bridge to efficiently populate the $^4F_{9/2}$ energy level, since these groups are capable of generating high energy vibration modes in the range of 3200 – 3600 1/cm, acting as a bridge between the $^2H_{11/2}/{}^4S_{3/2}$ and $^4F_{9/2}$ levels. This mechanism increases the probability of relaxation with the number of OH groups. In the end, the process decreases the number of radiative emissions in the green band, while increasing those in the red band [47,48]. Moreover, the use of 800 nm as excitation ensures minimal heating due to the absorption of the aqueous media, which directly improves the reliability of the sensor [49].

Several peaks associated with different transitions between the Nd^{3+} and Er^{3+} ions can be observed, but the main emissions from the Er^{3+} ions are of special interest. As we discussed, Er^{3+} ions present two main emissions in the green region, the first one around 525 nm, and the second one around 550 nm. Additionally, the $^4G_{7/2} \rightarrow {}^4I_{9/2}$ transition of Nd^{3+} overlaps with these green emissions, producing a final green band composed of both Er^{3+} and Nd^{3+} contributions. On the other hand, a second emission band can be observed in the red region of the spectrum, around 660 nm, which is composed of both emissions from Er^{3+} and Nd^{3+} ions, from their $^4F_{9/2} \rightarrow {}^4I_{15/2}$ and $^4G_{7/2} \rightarrow {}^4I_{15/2}$ transitions, respectively. An additional emission from Nd^{3+} ions can be observed around 580 nm, which originates from the $^4G_{7/2} \rightarrow {}^4I_{11/2}$ transition. The calculation of the D-glucose concentration will be based on the analysis of the red-to-green ratio of these bands.

3.2. *Detection of D-glucose with $NaGdF_4$: 5% Er^{3+}, 3% Nd^{3+} nanoparticles*

To demonstrate the sensing abilities of ErNd-NPs, a study of their visible emission in the presence of D-glucose was performed. As commented in **Section 3.1** , the main idea of this sensor is based on the energy match between the OH vibrational groups of D-glucose, with energies between 3200 and 3600 1/cm, and the energy separation between the $^2H_{11/2}/{}^4S_{3/2}$ and the $^4F_{9/2}$ levels (around 3200 1/cm). It is expected that the presence of D-glucose as ErNd-NPs produces a change in their visible emission, increasing the emissions associated with the red band (Er^{3+}: $^4F_{9/2} \rightarrow {}^4I_{15/2}$ + Nd^{3+}: $^4G_{7/2} \rightarrow {}^4I_{15/2}$), and decreasing the emissions associated with the green band (Er^{3+}: $^4S_{3/2} \rightarrow {}^4I_{15/2}$ + Nd^{3+}: $^4G_{7/2} \rightarrow {}^4I_{9/2}$), since the OH groups present in D-glucose are able to act as a bridge between the $^2H_{11/2}/{}^4S_{3/2}$ and the $^4F_{9/2}$ levels, increasing this way the probability of red emissions. The basic idea of the sensor is to measure the change in the red-to-green ratio in the presence of different concentrations of D-glucose.

Our first approach consists in binding D-glucose by electrostatic interactions to the surface of ligand-free ErNd-NPs to prove that the emission of the NPs changes with the presence of the molecule. To make the synthesised NPs dispersible in water, they were redispersed in an acidic medium under vigorous stirring in an overnight process, leading to the detachment of oleate from their surface. This process led to the protonation of the oleate ligands in the NPs, resulting in the removal of oleic acid from their surface [48]. Once the oleate from ErNd-NPs was removed, an aqueous dispersion of 10 mg/mL of ligand-free ErNd-NPs was prepared. After this, 2.5 mg of D-glucose were added to the NPs dispersion. The mixture was left overnight under stirring and then purified by centrifugation (10 min at 6000 RPM) to remove the excess of D-glucose. The resulting D-glucose/ErNd-NPs structures are expected to produce changes in the red-to-green fluorescence emission ratio of the NPs.

To demonstrate the presence of D-glucose on the surface of the NPs, dynamic light scattering (DLS), ζ-Potential, and Fourier transform spectroscopy (FTIR) measurements were performed. Fig. 2A shows the DLS measurements for oleate-coated ErNd-NPs, ligand-free ErNd-NPs and D-glucose/ErNd-NPs. A reduction in the diameter of ligand-free ErNd-NPs with respect to the one of oleate-coated ErNd-NPs can be observed, indicating successful removal of the oleate on the surface of the NPs. The original hydrodynamic diameter of the NPs was 110 ±

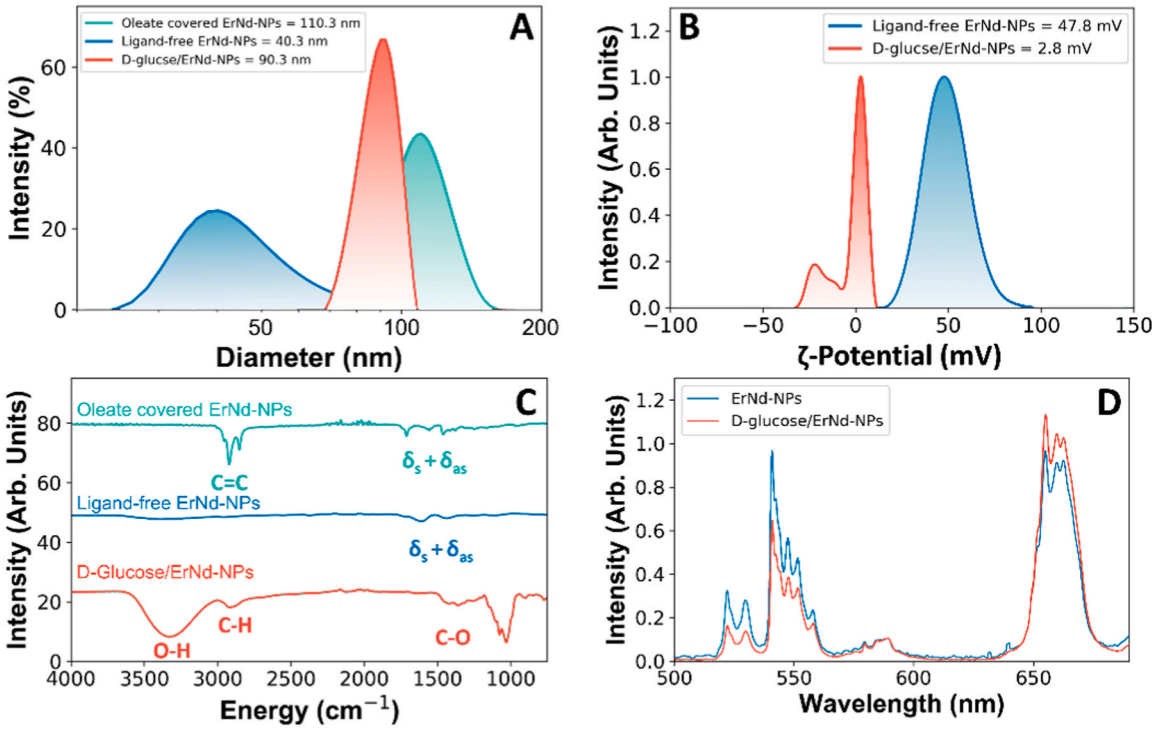

Fig. 2. A. Dynamic light scattering spectra for ErNd-NPs with (green) and without oleic acid (blue) and ErNd-NPs coated with D-glucose (red). B. ζ-Potential measurements (pH = 6.5) for ErNd-Nps without oleic acid (blue) and after the addition of D-glucose to their surface (red). C. FTIR spectra for oleate-covered ErNd-NPs (green), ligand-free ErNd-NPs (blue), and D-glucose/ErNd-NPs (red). D. Up-conversion emission spectrum of ErNd-NPs before (blue) and after (red) the addition of D-glucose.

18 nm, and after removing the oleate, the diameter was 40 ± 8 nm, which is in excellent agreement with the 31 ± 10 nm obtained from the analysis of TEM images. Once D-glucose is attached to the surface of the NPs, an increase in the diameter can be observed, with a value of 90 ± 10 nm, indicating a successful coating of the surface of ligand-free ErNd-NPs with D-glucose molecules. This result is the first proof of the interaction between D-glucose and ErNd-NPs.

The ζ-Potential values of the structures were measured in their different steps of preparation, and they can be consulted in Fig. 2**B**. Ligand-free ErNd-NPs show a positive surface charge, with a ζ-Potential value of 47.8 mV at a pH of 6.5, which is in agreement with other ζ-Potential studies performed with this type of NPs [50,51]. The reason behind the positive charge of these NPs is the abundance of positive ions (especially Gd^{3+}) on their surface, which become exposed once the oleate is removed from their surface. It has been reported that the pH of the solution in which the oleate is removed can directly affect the final charge of the NPs. When an acidic medium is used to promote the molecule protonation, oleic acid detaches from the surface of the NPs. From this point on, positive lanthanide ions on the surface can coordinate with water to produce lanthanide species ($Ln^{III}OH_2^+$), which present a positive charge [48]. The D-glucose/ErNd-NP presents a ζ-Potential value of 2.8 mV at a pH of 6.5, leading to the conclusion that D-glucose is reducing the ζ-Potential of the NPs, due to the possible interaction of the OH groups in D-glucose with the electrical double layer around the nanoparticle, leading to the formation of a self-assembled glucose monolayer that prevents direct interactions of ErNd-NPs with water.

Finally, FTIR measurements were performed to identify the vibrational modes associated with the different organic components in the samples. Fig. 2**C** shows the corresponding FTIR spectra for oleate-coated ErNd-NP, ligand-free ErNd-NP and D-glucose/ErNd-NP. The successful removal of the oleate on the ErNd-NPs can be observed, since the characteristic alkene stretchings (-C═C-) of oleic acid, at around 3000 1/cm, completely disappear. Two bands associated with the asymmetric (δ_s) and symmetric (δ_{as}) -COO stretching modes are still present in the FTIR spectrum of ligand-free ErNd-NPs at around 1465 and 1564 1/cm, respectively. It is believed that the presence of these bands is related to the adsorption of oleic acid molecules by the lanthanides in the system, since there is a coordination between the COO− group of oleic acid and the lanthanide ions [48,52], allowing for the presence of a small portion of oleic acid in the NPs even after the removal of the oleate from their surface. After the addition of D-glucose, two regions of low (500 – 1500 1/cm) and high (3000–3500 1/cm) frequency modes can be observed. The first one presents some bands related to C-O vibrations of D-glucose, whereas, for higher frequencies, a C-H band is located around 2970 1/cm, and a final band at 3470 1/cm associated with the OH vibrational modes of D-glucose can be observed [53–55]. The latter is responsible for the change in the red-to-green ratio of the studied NPs, since they can act as a bridge between energy levels, increasing the probability of red emissions.

Once the presence of D-glucose on the surface of ErNd-NPs has been tested, it is time to prove that the ratio of the visible emission of the NPs can change in the presence of D-glucose. Fig. 2D shows the visible emission of the ligand-free ErNd-NPs with (250 mg/dL) and without D-glucose (0 mg/dL). An evident change in the intensity of the peaks can be observed under direct Nd^{3+} excitation with an 800 nm laser. This clear decrease in the green emission of the NPs between 500 and 580 nm leads to a change in the red-to-green ratio. It is expected that if the green band decreases in intensity while the red band increases, the red/green ratio will increase with the concentration. This simple experiment helps to understand how the OH groups of D-glucose are reducing the population at the level that generates green emissions while increasing the red ones.

Additionally, an XPS analysis was performed to obtain a better understanding of the interaction between the D-glucose layer and the NPs. For this, 1 mg of D-glucose was added to a 1 mL aqueous dispersion of ErNd-NPs (10 mg/mL) to bind D-glucose to the NPs' surface. To prepare the samples, the D-glucose/ErNd-NPs were deposited on silicon substrates by drop casting, and they were introduced in an oven at 60 °C to

promote the evaporation of residual water. The same process was followed with ligand-free ErNd-NPs. Fig. 3A shows the XPS spectra of the ErNd-NPs before and after the addition of D-glucose. The high-resolution spectra for the O 1 s, C 1 s and Gd 4d core levels are also included in Fig. 3B, C and D, respectively. A quantification of the elements in the spectra showed in Fig. 3A was performed, and the results are shown in Table 1.

From this table, it can be observed that the main components of the sample before the addition of D-glucose are Na, Gd, and F, in concordance with the composition of the NPs. The presence of C and O before the addition of D-glucose can be considered as residual signals, but when D-glucose is added to the sample, the presence of C and O spikes due to their abundance in the composition of the molecule of D-glucose. As can be observed in Fig. 3A, the Gd $3d_{3/2}$ and $3d_{5/2}$ peaks suffer a significant attenuation after the addition of D-glucose, which is reflected in the atomic percentage of this element in Table 1.

Na 1s (Figure S1A) and F 1s (Figure S1B) core levels show a decrease in intensity associated with the attenuation of the signal substrate by the D-glucose layer. It is not expected to see very noticeable changes in the spectra mentioned above, since they correspond to the deeper core levels of Na and F atoms. On the contrary, the more external Ga 4d core levels are likely to show noticeable changes due to the possible chemical bond with the D-glucose molecule.

A weak signal was obtained for the core level of O 1s (Fig. 3B), and a slightly more intense one for the core level of C 1s (Fig. 3C) before the addition of D-glucose to the NPs, which may be attributed to the residual carbon and oxygen at the sample surface. The O 1s core level can be deconvoluted into two peaks that are commonly associated with C═O (lower BE) and C-O (higher BE) bonds. After the functionalisation with D-glucose, a clear increase in the intensity can be observed, which was an expected result due to oxygen in the D-glucose molecule. More importantly, a new component was found in higher BEs when analysing the shape of the O 1s core level, which may be indicative of a new chemical specie associated with the interaction of the NPs with the D-glucose layer [56,57]. The C 1s can be deconvoluted into three components. A main peak associated with C-C (sp^2) and C═C (sp^3) bonds, a second less intense contribution associated with C-O bonds, and a third peak at higher BEs, which can be straightforwardly related with the double bond between carbon and oxygen (C═O).

Table 1
XPS quantitative analysis of the surface components in the analysed samples before and after the addition of D-glucose.

Element	Atomic % before D-glucose	Atomic % after D-glucose
Sodium (Na)	11.7	1.2
Gadolinium (Gd)	13.5	5.4
Fluorine (F)	59.6	13.1
Carbon (C)	12.2	51.1
Oxygen (O)	3.0	20.1
Silicon (Si)	0.0	9.1

If the spectrum of the Gd 4d core level (Fig. 3D, on the top) is observed before the addition of D-glucose, two main features associated with the Gd $4d_{5/2}$ and Gd $4d_{3/2}$ spin-orbit splitting can be noticed. To obtain an analytical shape for this spectrum, it has been deconvoluted using four peaks as shown in Fig. 3D top. From this fitting, the ratios between the intensities and full widths at half maximum between the different peaks used, likewise their BE separation, are obtained. This information will be used later as a guide to define a reliable analytical shape of the new chemical species of Gd 4d that appear upon functionalisation with D-glucose. As soon as the NPs are functionalised with D-glucose, the spectrum becomes narrower, especially the Gd $4d_{5/2}$ core level, due to a decrease in sample charging. An extra peak can be observed at higher BEs, which is related to the Si 2s core level since a silicon substrate was used to deposit the samples. During the XPS measurements of the sample containing D-glucose, it was observed that, under ultra-high vacuum, the NPs + D-glucose on the surface tend to move towards the borders of the substrate, related to a change in the vicinity of D-glucose because of the reduction of the pressure. This effect

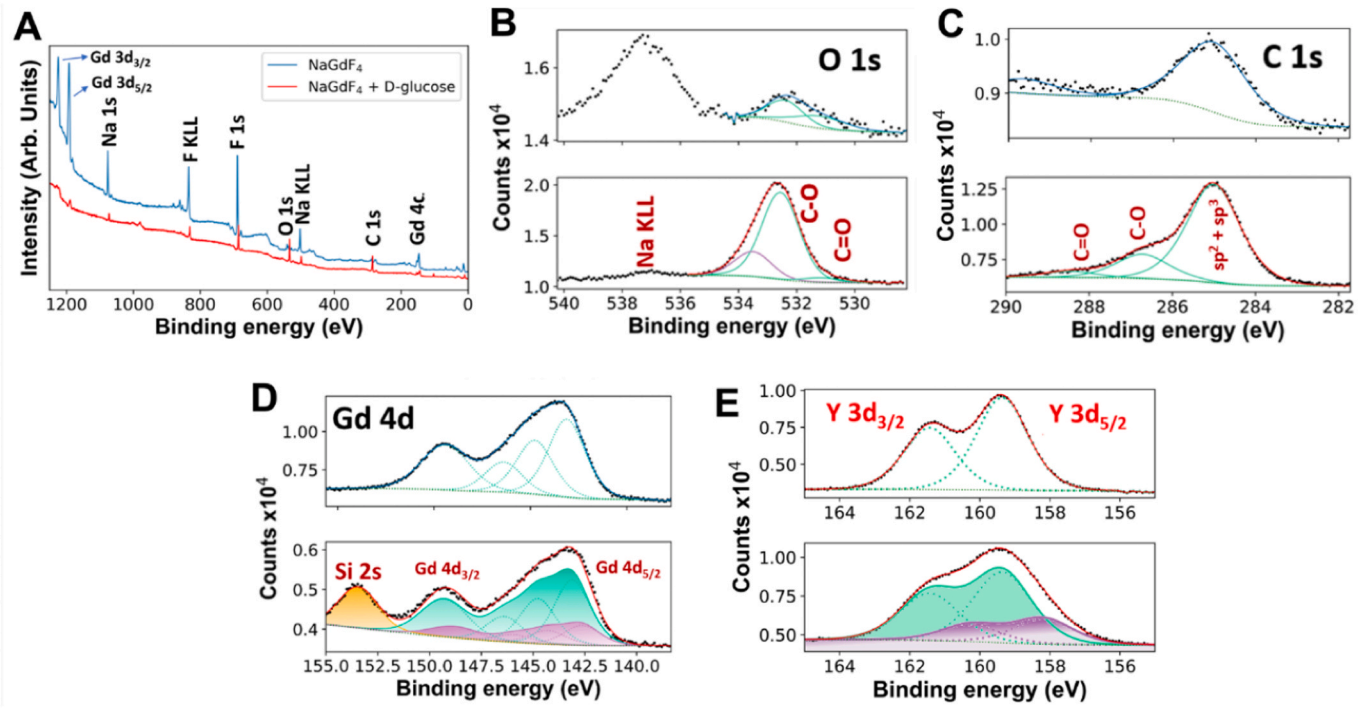

Fig. 3. A. XPS spectrum of ErNd-NPs B., C. and D. High-resolution spectra for the O 1 s, C 1 s and Gd 4d core levels, respectively, of ErNd-NPs. E. High-resolution spectra of the Y 3d core level of non-functionalised (up) and polyacrylic acid-functionalised (bottom) of $NaYF_4$ NPs. Black dots represent the raw data, while blue and red lines represent the corresponding envelopes before and after the addition of D-glucose, respectively. The green dotted line represents the background, and the green cyan and magenta lines represent the different components of the spectra.

did not prevent results from being obtained, but it did cause the apparition of Si peaks in the spectrum as a result of the displacement of the NPs + D-glucose in some areas of the Si substrate. Therefore, this peak does not provide useful extra information about the interaction between the NPs and D-glucose. By analysing in detail the Gd 4d core level, significant changes can be observed, in addition to the above-mentioned narrowing of the spectrum. To analyse the shape of the core level, a new reliable set of four peaks (magenta) must be introduced at lower BEs (Fig. 3D bottom). Therefore, two sets of four peaks are observed when reproducing the shape of the Gd 4d core level upon D-glucose functionalisation. The first one (green cyan) related to Gd atoms not bonded to D-glucose, and the second one (magenta) associated with Gd atoms bonded to D-glucose. From this analysis, a shift of 0.6 eV to lower BEs of the Gd $4d_{5/2}$ and Gd $4d_{3/2}$ core levels, respectively, is observed. A similar result was obtained in a parallel study carried out involving the functionalisation of $NaYF_4$ NPs doped with Er^{3+} and Yb^{3+} with polyacrylic acid. The interaction between the surface of the NPs and polyacrylic acid is a well-known process that helps to understand what may be happening with D-glucose. Fig. 3E shows the Y 3d core level of ligand-free $NaYF_4$ NPs (up). This spectrum can be fitted by two peaks (green cyan) associated with the Y $3d_{5/2}$ and $3d_{3/2}$ spin-orbit splitting. In contrast, upon functionalization of the NPs with polyacrylic acid (down), significant changes are observed in the Y 3d spectrum, which could be related to the formation of new chemical species on the surface associated with the interaction of the NPs with polyacrylic acid. Conforming the shape of the Y 3d core level upon polyacrylic acid functionalisation, an additional Y 3d doublet at lower BEs is observed, indicating a possible new chemical species associated with the presence of the polymer. This new doublet is shifted by 1.1 eV to lower BEs with respect to that observed in the non-functionalised $NaYF_4$ NPs. There are previous studies on such core levels that conclude that changes in the shape and BE of the core levels may be an indication of new chemical species or significant changes in the surface of the analysed sample [58,59]. This result resembles the one obtained in this work when the Gd 4d core level is analysed in detail.

3.3. Detection of D-glucose in paper substrates

The next step of the study consists of the NPs to be tested on paper substrates. For this purpose, paper-based sensors containing ErNd-NPs were prepared following protocol by Mei *et al.* [60] described in **Section 2.7** . Once the paper-based sensor was ready, different solutions of D-glucose in deionised water were prepared, ranging from 0 to 200 mg/dL. The paper-based sensors containing ErNd-NPs were submerged for 60 s in the different D-glucose solutions and then dried. Finally, the emission spectrum of four different regions of the paper-based sensors was measured in order to have a mean value of several measurements. No remarkable changes between the spectrum shape of the NPs in the dispersion and the ones in the paper substrate were observed. Fig. 4A shows the red-peak-normalised spectra of ErNd-NPs in the paper-based sensor for the minimum and maximum concentrations of D-glucose.

The spectrum was taken using an 800 nm diode laser as a source of excitation. As it can be observed, the green band associated with the Er^{3+}: $^4S_{3/2} \rightarrow {}^4I_{15/2}$ and Nd^{3+}: $^4G_{7/2} \rightarrow {}^4I_{9/2}$ transitions reduce its intensity with increasing concentration of D-glucose. Further analysis of the red-to-green ratio (calculated with the area under the green and red bands) shows a linear trend with the concentration of D-glucose, as can be consulted in Fig. 4B. As it was expected, the red-to-green ratio increases with the concentration of D-glucose. The analysis of the ratio and the concentration of D-glucose follows a linear tendency given by Eq. 1:

$$Ratio_{red/green} = 0.0022[C] + 1.36 \quad (1)$$

Here [C] represents the concentration of D-glucose expressed in mg/dL. The limit of detection (LOD) is defined as the minimum concentration of analyte that a sensor can detect with reasonable certainty, and it was calculated using the model proposed by Foley et al. [61], given by Eq. 2.

$$LOD = 3\sigma_{std}/m \quad (2)$$

Where σ_{std} is the standard deviation of 10 consecutive measurements of the blank sensor (only containing ErNd-NPs) and m is the slope of the calibration curve previously shown in Eq. 1. Subsequently, a limit of detection of 22 mg/dL was obtained, which is an excellent result, since it has been reported that the standard tear glucose concentration has been reported in non-diabetic patients that range from 0 to 65 mg/dL, while in diabetic patients concentrations as high as 84 mg/dL have been detected [11]. Moreover, the obtained LOD is in the expected range of sensors containing rare-earth ions [62] and rare-earth-doped nanoparticles [63], but with the added benefit of offering not only a more direct method of detection, but also a simpler fabrication process, which is also, to the limit of our knowledge, one of the first times developing a glucose paper-based sensor using rare-earth-doped nanoparticles.

4. Conclusions

In this work, the sensing ability of 31 nm $NaGdF_4$: 5% Er^{3+}, 3% Nd^{3+} towards D-glucose was demonstrated. First, a study of the interaction between the NPs and D-glucose was performed, and proofs of this interaction were presented through DLS, ζ-Potential, FTIR and XPS measurements with optimal results. The detection mechanism of D-glucose was tested, demonstrating that a dispersion of these NPs presented changes in the green band of the up-conversion emission in the presence of D-glucose, which proved their sensing abilities. After this, the NPs were successfully deposited in paper substrates, and different concentrations of D-glucose were used to test the sensor, successfully

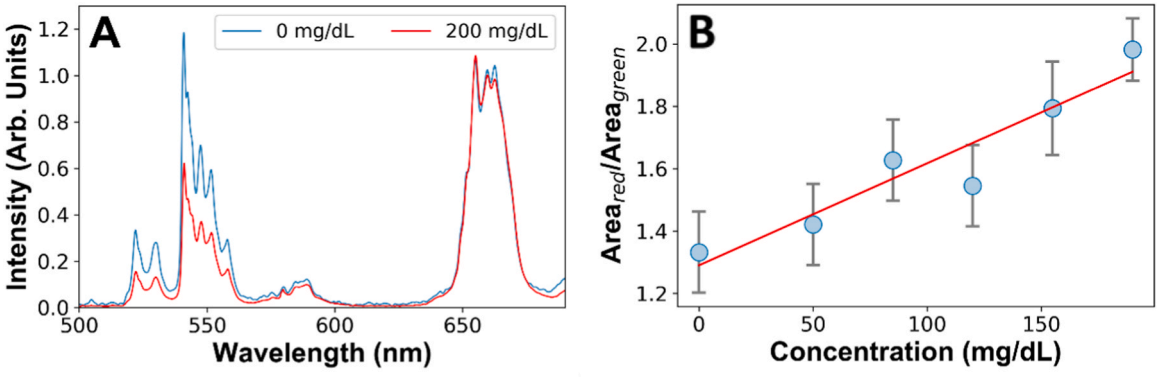

Fig. 4. A. Visible emission spectra of paper-based sensors containing ErNd-NPs for the minimum and maximum used concentrations of D-glucose. B. Calibration curve of the red-to-green ratio.

observing changes in the red-to-green ratio of the NPs for each concentration. With these results, a calibration model for the detection of D-glucose concentrations ranging from 0 to 200 mg/dL was obtained. A paper-based enzyme-free luminescence sensor was successfully manufactured for the detection of D-glucose based on changes in the emission of ErNd-NPs was successfully fabricated, with a detection limit of 22 mg/dL.

Funding

This work was financed by Comunidad de Madrid and Universidad Autónoma de Madrid (Project SI3/PJI/2021-00211). Additional funding was received by Grant PID2019-106211RB-I00 (NANONERV) and Grant PID2020-118878RB-I00 (RETINanoTHERMIA) by MCIN/AEI/10.13039/501100011033. Financial support from grant PID2020-116712RB-C21 funded by MCIN/AEI/10.13039/501100011033 is acknowledged by A.A. and from grant PID2020-112770RB-C22 funded by the same program is acknowledged by M.M.

CRediT authorship contribution statement

Miguel Manso Silvan: Writing – review & editing, Supervision. **Antonio Arranz:** Writing – review & editing, Investigation, Data curation. **Nicoleta Bogdan:** Writing – review & editing. **Gabriel López-Peña:** Writing – review & editing, Writing – original draft, Investigation, Formal analysis, Data curation. **Eva Ortiz-Mansilla:** Writing – review & editing, Investigation, Data curation. **Emma Martín Rodríguez:** Writing – review & editing, Supervision, Project administration, Funding acquisition, Conceptualization.

Declaration of Competing Interest

The authors declare that they have no known competing financial interests or personal relationships that could have appeared to influence the work reported in this paper.

Data availability

Data will be made available on request.

Appendix A. Supporting information

Supplementary data associated with this article can be found in the online version at doi:10.1016/j.colsurfb.2024.113934.

References

[1] D. Bruen, C. Delaney, L. Florea, D. Diamond, Glucose sensing for diabetes monitoring: Recent developments, Sensors 17 (2017), https://doi.org/10.3390/s17081866.
[2] I. Conget, P UESTA AL D ÍA Diabetes y enfermedades cardiovasculares (I) Diagnóstico, clasificación y patogenia de la diabetes mellitus Sección patrocinada por el Laboratorio Dr. Esteve, 2002.
[3] I. Abe, F. Islam, A.K.-Y. Lam, Glucose intolerance on phaeochromocytoma and paraganglioma—the current understanding and clinical perspectives, Front. Endocrinol. 11 (2020), https://doi.org/10.3389/fendo.2020.593780.
[4] L.-W. Zhang, M.-H. Ruan, J.-L. Liu, C.-H. He, J.-R. Yu, Progress on research and development in diabetes mellitus, Yi Chuan 44 (2022) 824–839, https://doi.org/10.16288/j.yczz.22-272.
[5] P.E. Cryer, Hypoglycemia, functional brain failure, and brain death, J. Clin. Investig. 117 (2007), https://doi.org/10.1172/JCI31669.
[6] D. Giugliano, A. Ceriello, K. Esposito, Glucose metabolism and hyperglycemia, : Am. J. Clin. Nutr. (2008), https://doi.org/10.1093/ajcn/87.1.217s.
[7] Santiago Campillo, Hiperglucemia e hipoglucemia: causas, síntomas y tratamiento, (2022). ⟨https://www.vitonica.com/enfermedades/hiperglucemia-e-hipoglucemia-causas-sintomas-tratamiento⟩ (accessed February 13, 2023).
[8] Mayo Clinic, Hiperglucemia en la diabetes - Síntomas y causas, (2022). ⟨https://www.mayoclinic.org/es-es/diseases-conditions/hyperglycemia/symptoms-causes/syc-20373631⟩ (accessed February 13, 2023).
[9] Mayo Clinic, Hipoglucemia diabética - Síntomas y causas, (2022). ⟨https://www.mayoclinic.org/es-es/diseases-conditions/diabetic-hypoglycemia/symptoms-causes/syc-20371525⟩ (accessed February 13, 2023).
[10] M.B. Davidson, Historical review of the diagnosis of prediabetes/intermediate hyperglycemia: case for the international criteria, Diabetes Res. Clin. Pract. 185 (2022) 109219, https://doi.org/10.1016/j.diabres.2022.109219.
[11] J.T. Baca, D.N. Finegold, S.A. Asher, Tear glucose analysis for the noninvasive detection and monitoring of diabetes mellitus, Ocul. Surf. 5 (2007), https://doi.org/10.1016/S1542-0124(12)70094-0.
[12] J.D. Lane, D.M. Krumholz, R.A. Sack, C. Morris, Tear glucose dynamics in diabetes mellitus, Curr. Eye Res. 31 (2006), https://doi.org/10.1080/02713680600976552.
[13] J. T, S. R, R. J, A. Poojha, Novel Approach to Non-Invasive Blood Glucose Monitoring Based on Visible Laser Light, in: 2022 International Conference on Automation, Computing and Renewable Systems (ICACRS), 2022: pp. 54–57. ⟨https://doi.org/10.1109/ICACRS55517.2022.10029239⟩.
[14] K.E. Shafer-Peltier, C.L. Haynes, M.R. Glucksberg, R.P. Van Duyne, Toward a glucose biosensor based on surface-enhanced Raman scattering, J. Am. Chem. Soc. 125 (2003), https://doi.org/10.1021/ja028255v.
[15] X. Sun, Glucose detection through surface-enhanced Raman spectroscopy: a review, Anal. Chim. Acta 1206 (2022) 339226, https://doi.org/10.1016/j.aca.2021.339226.
[16] J.W. Kang, Y.S. Park, H. Chang, W. Lee, S.P. Singh, W. Choi, L.H. Galindo, R. R. Dasari, S.H. Nam, J. Park, P.T.C. So, Direct observation of glucose fingerprint using in vivo Raman spectroscopy, Sci. Adv. 6 (2020) eaay5206, https://doi.org/10.1126/sciadv.aay5206.
[17] Noninvasive glucose monitoring using polarized light | Proceedings of the 18th Conference on Embedded Networked Sensor Systems, (n.d.). ⟨https://dl.acm.org/doi/abs/10.1145/3384419.3430720⟩ (accessed March 12, 2024).
[18] M. Shokrekhodaei, S. Quinones, Review of non-invasive glucose sensing techniques: optical, electrical and breath acetone, Sensors 20 (2020) 1251, https://doi.org/10.3390/s20051251.
[19] Real-time compensation method for robust polarimetric determination of glucose in turbid media, (n.d.). ⟨https://opg.optica.org/boe/fulltext.cfm?uri=boe-10-1-308&id=403265⟩ (accessed March 12, 2024).
[20] P. Mukherjee, N. Hagen, Y. Otani, Glucose sensing in the presence of scattering by analyzing a partial Mueller matrix, Optik 180 (2019) 775–781, https://doi.org/10.1016/j.ijleo.2018.11.157.
[21] H.A. MacKenzie, H.S. Ashton, S. Spiers, Y. Shen, S.S. Freeborn, J. Hannigan, J. Lindberg, P. Rae, Advances in photoacoustic noninvasive glucose testing, Clin. Chem. (1999), https://doi.org/10.1093/clinchem/45.9.1587.
[22] K.V. Larin, M.S. Eledrisi, M. Motamedi, R.O. Esenaliev, Noninvasive blood glucose monitoring with optical coherence tomography: a pilot study in human subjects, Diabetes Care 25 (2002), https://doi.org/10.2337/diacare.25.12.2263.
[23] T. Miura, A. Seiyama, M. Cassim, J. Seki, Improved accuracy of tissue glucose measurement using low magnification optical coherence tomography, IEEE Sens. Lett. 5 (2021) 1–4, https://doi.org/10.1109/LSENS.2021.3126431.
[24] I. Ahmed, N. Jiang, X. Shao, M. Elsherif, F. Alam, A. Salih, H. Butt, A.K. Yetisen, Recent advances in optical sensors for continuous glucose monitoring, Sens. Diagn. 1 (2022) 1098–1125, https://doi.org/10.1039/D1SD00030F.
[25] K. Aslan, J.R. Lakowicz, C.D. Geddes, Nanogold-plasmon-resonance-based glucose sensing, Anal. Biochem. 330 (2004), https://doi.org/10.1016/j.ab.2004.03.032.
[26] N. Mudgal, A. Saharia, A. Agarwal, J. Ali, P. Yupapin, G. Singh, Modeling of highly sensitive surface plasmon resonance (SPR) sensor for urine glucose detection, Opt. Quant. Electron 52 (2020) 307, https://doi.org/10.1007/s11082-020-02427-0.
[27] B. Karki, A. Jha, A. Pal, V. Srivastava, Sensitivity enhancement of refractive index-based surface plasmon resonance sensor for glucose detection, Opt. Quant. Electron 54 (2022) 595, https://doi.org/10.1007/s11082-022-04004-z.
[28] A. Caduff, E. Hirt, Y. Feldman, Z. Ali, L. Heinemann, First human experiments with a novel non-invasive, non-optical continuous glucose monitoring system, Biosens. Bioelectron. 19 (2003), https://doi.org/10.1016/S0956-5663(03)00196-9.
[29] J. Huang, Y. Zhang, J. Wu, Review of non-invasive continuous glucose monitoring based on impedance spectroscopy, Sens. Actuators A Phys. 311 (2020) 112103, https://doi.org/10.1016/j.sna.2020.112103.
[30] B.G. Pedro, D.W.C. Marcôndes, P. Bertemes-Filho, Analytical model for blood glucose detection using electrical impedance spectroscopy, Sensors 20 (2020) 6928, https://doi.org/10.3390/s20236928.
[31] J.C. Pickup, F. Hussain, N.D. Evans, N. Sachedina, In vivo glucose monitoring: the clinical reality and the promise, Biosens. Bioelectron. (2005), https://doi.org/10.1016/j.bios.2004.08.016.
[32] Y. Cui, W. Duan, Y. Jin, F. Wo, F. Xi, J. Wu, Ratiometric fluorescent nanohybrid for noninvasive and visual monitoring of sweat glucose, ACS Sens 5 (2020) 2096–2105, https://doi.org/10.1021/acssensors.0c00718.
[33] T.V. Tam, S.H. Hur, J.S. Chung, W.M. Choi, Novel paper- and fiber optic-based fluorescent sensor for glucose detection using aniline-functionalized graphene quantum dots, Sens. Actuators B: Chem. 329 (2021) 129250, https://doi.org/10.1016/j.snb.2020.129250.
[34] P. Ravishankar, A. Daily, Tears as the next diagnostic biofluid: a comparative study between ocular fluid and blood, Appl. Sci. 12 (2022) 2884, https://doi.org/10.3390/app12062884.
[35] A.C. Raposo, R.D. Portela, M. Aldrovani, T.D. Barral, D. Cury, A.P. Oriá, Comparative analysis of tear composition in humans, domestic mammals, reptiles, and birds, Front. Vet. Sci. 7 (2020), https://doi.org/10.3389/fvets.2020.00283.
[36] F. Bachhuber, A. Huss, M. Senel, H. Tumani, Diagnostic biomarkers in tear fluid: from sampling to preanalytical processing, Sci. Rep. 11 (2021) 10064, https://doi.org/10.1038/s41598-021-89514-8.
[37] G. Kalló, M. Emri, Z. Varga, B. Ujhelyi, J. Tőzsér, A. Csutak, É. Csősz, Changes in the chemical barrier composition of tears in Alzheimer's disease reveal potential tear diagnostic biomarkers, PLoS One 11 (2016) e0158000, https://doi.org/10.1371/journal.pone.0158000.

[38] S. Hagan, E. Martin, A. Enríquez-de-Salamanca, Tear fluid biomarkers in ocular and systemic disease: potential use for predictive, preventive and personalised medicine, EPMA J. 7 (2016) 15, https://doi.org/10.1186/s13167-016-0065-3.
[39] A. Barmada, S.A. Shippy, Tear analysis as the next routine body fluid test, Eye 34 (2020) 1731–1733, https://doi.org/10.1038/s41433-020-0930-0.
[40] T. Näreoja, T. Deguchi, S. Christ, R. Peltomaa, N. Prabhakar, E. Fazeli, N. Perälä, J. M. Rosenholm, R. Arppe, T. Soukka, M. Schäferling, Ratiometric sensing and imaging of intracellular pH using polyethylenimine-coated photon upconversion nanoprobes, Anal. Chem. 89 (2017) 1501–1508, https://doi.org/10.1021/acs.analchem.6b03223.
[41] X. Liu, Y. Yang, X. Xing, Y. Wang, Grey level replaces fluorescent intensity: fluorescent paper sensor based on ZnO nanoparticles for quantitative detection of Cu2+ without photoluminescence spectrometer, Sens. Actuators, B: Chem. 255 (2018), https://doi.org/10.1016/j.snb.2017.09.044.
[42] M. Runowski, P. Woźny, V. Lavín, S. Lis, Optical pressure nano-sensor based on lanthanide doped SrB2O4:Sm2+ luminescence – novel high-pressure nanomanometer, Sens. Actuators B: Chem. 273 (2018) 585–591, https://doi.org/10.1016/j.snb.2018.06.089.
[43] S. Shinoda, H. Miyake, H. Tsukube, Molecular recognition and sensing via rare earth complexes, Handb. Phys. Chem. Rare Earths (2005), https://doi.org/10.1016/S0168-1273(05)35004-5.
[44] P.J. Bracher, M. Gupta, G.M. Whitesides, Patterning precipitates of reactions in paper, J. Mater. Chem. 20 (2010), https://doi.org/10.1039/c000358a.
[45] S.-T. Han, H. Peng, Q. Sun, S. Venkatesh, K.-S. Chung, S.C. Lau, Y. Zhou, V.A. L. Roy, An overview of the development of flexible sensors, Adv. Mater. 29 (2017) 1700375, https://doi.org/10.1002/adma.201700375.
[46] M. Segev-Bar, H. Haick, Flexible sensors based on nanoparticles, ACS Nano 7 (2013) 8366–8378, https://doi.org/10.1021/nn402728g.
[47] S. Zheng, W. Chen, D. Tan, J. Zhou, Q. Guo, W. Jiang, C. Xu, X. Liu, J. Qiu, Lanthanide-doped NaGdF $_4$ core–shell nanoparticles for non-contact self-referencing temperature sensors, Nanoscale 6 (2014) 5675–5679, https://doi.org/10.1039/C4NR00432A.
[48] N. Bogdan, F. Vetrone, G.A. Ozin, J.A. Capobianco, Synthesis of ligand-free colloidally stable water dispersible brightly luminescent lanthanide-doped upconverting nanoparticles, Nano Lett. (2011), https://doi.org/10.1021/nl1041929.
[49] T. Muñoz-Ortiz, L. Abiven, R. Marin, J. Hu, D.H. Ortgies, A. Benayas, F. Gazeau, V. Castaing, B. Viana, C. Chanéac, D. Jaque, F.E. Maturi, L.D. Carlos, E. Martín Rodríguez, J. García Solé, Temperature dependence of water absorption in the biological windows and its impact on the performance of Ag2S luminescent nanothermometers, Part. Part. Syst. Charact. 39 (2022), https://doi.org/10.1002/ppsc.202200100.
[50] C. Liu, D. Lu, X. You, G. Shi, J. Deng, T. Zhou, Carbon dots sensitized lanthanide infinite coordination polymer nanoparticles: towards ratiometric fluorescent sensing of cerebrospinal Aβ monomer as a biomarker for Alzheimer's disease, Anal. Chim. Acta 1105 (2020), https://doi.org/10.1016/j.aca.2020.01.021.
[51] J. Tian, X. Zeng, X. Xie, S. Han, O.W. Liew, Y.T. Chen, L. Wang, X. Liu, Intracellular adenosine triphosphate deprivation through lanthanide-doped nanoparticles, J. Am. Chem. Soc. 137 (2015), https://doi.org/10.1021/jacs.5b00981.
[52] K. Yang, H. Peng, Y. Wen, N. Li, Re-examination of characteristic FTIR spectrum of secondary layer in bilayer oleic acid-coated Fe 3 O 4 nanoparticles, Appl. Surf. Sci. 256 (2010), https://doi.org/10.1016/j.apsusc.2009.11.079.
[53] K. Kaminski, E. Kaminska, K. Adrjanowicz, Z. Wojnarowska, P. Wlodarczyk, K. Grzybowska, M. Dulski, R. Wrzalik, M. Paluch, Observation of the dynamics of clusters in d-glucose with the use of dielectric spectroscopy, Phys. Chem. Chem. Phys. 12 (2010), https://doi.org/10.1039/b916699h.
[54] Docbrown, Docbrown, (2022). ⟨https://www.docbrown.info/page06/spectra2/d-glucose-ir.htm⟩ (accessed January 24, 2023).
[55] L. Xu, X.C. Wu, J.J. Zhu, Green preparation and catalytic application of Pd nanoparticles, Nanotechnology 19 (2008), https://doi.org/10.1088/0957-4484/19/30/305603.
[56] K. Vasuki, G. Siva, A. Balasubramani, M. Pannipara, A.G. Al-Sehemi, Y. Xia, R. Fang, D.J. Yoo, T.R. Kumar, R. Ramachandran, G. Gnana kumar, Surfactant and binder free hierarchical NCNPs@CuO nanostructures on ITO for the cost effective enzyme-free glucose sensor applications, Appl. Phys. A 125 (2019) 384, https://doi.org/10.1007/s00339-019-2652-3.
[57] S. Nabih, S.S. Hassn, Chitosan-capped Ag–Au/rGO nanohybrids as promising enzymatic amperometric glucose biosensor, J. Mater. Sci. Mater. Electron. 31 (2020) 13352–13361, https://doi.org/10.1007/s10854-020-03889-4.
[58] T. Mongstad, A. Thøgersen, A. Subrahmanyam, S. Karazhanov, The electronic state of thin films of yttrium, yttrium hydrides and yttrium oxide, Sol. Energy Mater. Sol. Cells 128 (2014), https://doi.org/10.1016/j.solmat.2014.05.037.
[59] L. Mai, N. Boysen, E. Subaşı, T. de los Arcos, D. Rogalla, G. Grundmeier, C. Bock, H.-L. Lu, A. Devi, Water assisted atomic layer deposition of yttrium oxide using tris (*N*, *N* ′-diisopropyl-2-dimethylamido-guanidinato) yttrium(<scp>iii</scp>): process development, film characterization and functional properties, RSC Adv. 8 (2018) 4987–4994, https://doi.org/10.1039/C7RA13417G.
[60] Q. Mei, H. Jing, Y. Li, W. Yisibashaer, J. Chen, B. Nan Li, Y. Zhang, Smartphone based visual and quantitative assays on upconversional paper sensor, Biosens. Bioelectron. 75 (2016), https://doi.org/10.1016/j.bios.2015.08.054.
[61] J.P. Foley, J.G. Dorsey, Clarification of the limit of detection in chromatography, Chromatographia 18 (1984), https://doi.org/10.1007/BF02267236.
[62] S.B. Jadhav, U.M. Patil, R.N. Bulakhe, I. In, C.D. Lokhande, P.N. Pawaskar, Vertically aligned nanosheets of an electrodeposited lanthanum oxide electrode for non-enzymatic glucose sensing application, J. Electron. Mater. 50 (2021) 675–685, https://doi.org/10.1007/s11664-020-08605-w.
[63] M. Wang, B. Lin, Y. Chen, H. Liu, Z. Ju, R. Lv, Fluorescence-recovered wearable hydrogel patch for in vitro detection of glucose based on rare-earth nanoparticles, ACS Biomater. Sci. Eng. 10 (2024) 1128–1138, https://doi.org/10.1021/acsbiomaterials.3c01682.